



Cite this: *CrystEngComm*, 2022, 24, 3338

Structural transitions during the water sorption process in two layered metal hydrogen-bonded organic frameworks and the effect of the H-bond strength between the layers†

Patrice Kenfack Tsobnang,^a Yannick Thiery Sakam Nchedoung,^a Dominik Fröhlich,^b Florence Porcher,^c Lina Rustam,^b Emrah Hastürk^d and Christoph Janiak^d

The supramolecular network material [Co(amp)₃][Cr(ox)₃] (amp = 2-aminomethylpyridine, ox = oxalate) (I') shows in its powder X-ray diffraction (PXRD) carpet plot during the water adsorption process two sets of diffraction lines related to its structure and to that of [Co(amp)₃][Cr(ox)₃·6H₂O] (I) having the same symmetry (space group $P2_1/n$). The first set occurs in the range of 0 to 39% relative humidity (r.H.), and the second set is observed in the range of 30 to 90% r.H. During the desorption process, this second set is observed from 90 to 5% r.H., and the first set in the range of 15 to 0% r.H. indicating that the stepped water sorption isotherm and the large hysteresis loop for this material are coordinated with the discontinuous phase transitions occurring with water adsorption–desorption on this material. During these transitions, the rate of conversion depends on the water pressure in the system, and the structural change is mainly observed along the *b*-axis, which is the stacking direction of the layers. The same observations are made for the supramolecular material [Cu₂(amp)₄Cl][Cr(ox)₃·1H₂O] (II'), which is converted to [Cu₂(amp)₄Cl][Cr(ox)₃·6H₂O] (II) during the water adsorption process. But in this case, the discontinuous phase transition starts at 10% r.H. during both the adsorption and desorption processes, and lens-shaped diffraction lines are observed in the range of 10 and 90% r.H. indicating a continuous phase transition in this range. During the discontinuous phase transition, the space group of the framework is changed from $P2_1/n$ to $C2/c$, and the latter is maintained during the continuous phase transition. The lens-shaped diffraction lines are related to the gradual increase of the *b* parameter (stacking direction of layers) with increasing humidity. The hydrogen bonds found in the bilayer space of I' are stronger than those found in that of II', which explains the abrupt transition in the former compared to the continuous phase transition in II' and the higher quantity of water adsorbed in I' compared to that of II' during the gate effect.

Received 28th January 2022,
Accepted 16th March 2022

DOI: 10.1039/d2ce00138a

rsc.li/crystengcomm

Introduction

Porous materials are compounds which have cavities able to adsorb species from the environment. Porous matter can be designed with a judicious choice of entities commonly called 'building units' which are assembled through suitable topologies.^{1,2} Depending on the type of interactions used, three classes of porous materials are defined: the metal-organic frameworks (MOFs), also called porous coordination polymers, in which the units are connected through coordinative bonds;^{3,4} the covalent organic frameworks (COFs),^{5,6} in which the covalent bonds are used; and the porous supramolecular networks (PSN) or porous supramolecular materials, which include hydrogen-bonded organic frameworks (HOFs),^{7–9} Metal hydrogen-bonded organic frameworks (M-HOFs) and π -frameworks.^{10–15} The

^a University of Dschang, Department of Chemistry, PO Box 67, Dschang, Cameroon. E-mail: pakenfack@gmail.com, patrice.kenfack@univ-dschang.org

^b Fraunhofer-Institut for Solar Energy Systems ISE, Division Thermal Systems and Buildings, Heidenhofstraße 2, 79110 Freiburg, Germany

^c Laboratoire Léon Brillouin (LLB), UMR 12 CEA/CNRS, Bât. 563 CEA Saclay, 91191 Gif-sur-Yvette cedex, France

^d Institut für Anorganische Chemie und Strukturchemie, Heinrich-Heine-Universität Düsseldorf, Universitätsstraße 1, 40225 Düsseldorf, Germany. E-mail: janiak@uni-duesseldorf.de

† Electronic supplementary information (ESI) available: Section 1. Packing diagrams and characteristics of the hydrogen bonds of I' and II'; Section 2. Synthesis of I and II; Section 3. Crystal data of the materials and confirmation of the synthesis of I and II; Section 4. Elemental analysis of I and II; Section 5. Lattice parameters of the two materials at the studied humidity levels; Section 6. Powder diffraction patterns of I'/I during the discontinuous phase transitions. See DOI: <https://doi.org/10.1039/d2ce00138a>

porous supramolecular material class is less developed compared to the other two, but it has been receiving increasing attention in the last five years. The building units in HOFs, MOF-HOFs and π -frameworks are connected with comparatively weak interactions (hydrogen bonds, π - π interactions, weak coordinative bonds, *etc.*), and these weak interactions can contribute to the flexibility of the resulting frameworks.

Kitagawa *et al.* (1998) defined three generations of porous materials according to their behaviour upon sorption processes.¹⁶ The first generation includes materials whose architecture collapses upon desolvation, while the second generation are materials that have a rigid architecture and permanent porosity. The materials having dynamic frameworks sensitive to an external stimulus such as light, temperature, electric field, gas molecules, *etc.* constitute the third generation. Manifestations of the flexibility of third generation porous materials are: swelling,¹⁷ gate opening,¹⁸ breathing,^{19,20} linker rotation,²¹ expansion/shrinkage of bilayer regions, *etc.* Owing to this flexibility, third generation porous materials can be very efficient for applications, like heat transformation processes,^{22,23} autonomous indoor humidity control,^{24,25} gas separations,^{26,27} *etc.* The gate opening/closing processes followed by a steep gas adsorption/desorption (indicated by an S-shaped isotherm) are very important for these applications since they offer the potential for selective and pressure swing adsorptions. Materials having stacked layered frameworks are good candidates for these properties, especially when their porosity is accessible *via* expansion of their interlayer regions.

To rationally design these materials for specific applications, many studies are carried out, and some important aspects are the determination of driving parameters of their flexibility and the relationship of these parameters with the flexibility mode occurring in these materials. Many parameters related to the sorption process, the guest and the host framework have been reported to date.^{26,28–34} In the contribution to these studies, the structural changes occurring in the architecture of the supramolecular structures of $[\text{Co}(\text{amp})_3][\text{Cr}(\text{ox})_3]$ (**I'**) (Fig. 1a and 2a and b) and $[\text{Cu}_2(\text{amp})_4\text{Cl}][\text{Cr}(\text{ox})_3]\cdot\text{H}_2\text{O}$ (**II'**) (Fig. 1b

and 2c and d) during their water sorption processes are reported in this work.

Both materials have non-porous architectures with stacked corrugated layers (see Fig. S1 and S2 of section 1 of the ESI†) which adsorb water molecules with an S-shaped isotherm having a hysteresis loop between 10 and 30% relative humidity (r.H.) for **I'** and no hysteresis loop for **II'**.²⁴ The quantities of water vapor molecules contributing to the steep adsorption branches of their isotherm are 117 mg g^{-1} for **I'** and 41 mg g^{-1} for **II'**. During the adsorption process, **I'** is converted to $[\text{Co}(\text{amp})_3][\text{Cr}(\text{ox})_3]\cdot 6\text{H}_2\text{O}$ (**I**) (Fig. 2a \rightarrow b) with a discontinuous phase transition, while the conversion of **II'** to $[\text{Cu}_2(\text{amp})_4\text{Cl}][\text{Cr}(\text{ox})_3]\cdot 6\text{H}_2\text{O}$ (**II**) (Fig. 2c \rightarrow d) occurs *via* the succession of one discontinuous and one continuous phase transitions. All these differences could be ascribed to the strength of the interactions between the layers in both materials. To the best of our knowledge, to date this effect was only reported by Roztocki *et al.* for CO_2 sorption on the 2D isophthalic- and 5-aminoisophthalic-MOFs, and infrared analyses with an assumption on the structure of activated materials (not obtained) were used for elucidation.³⁴ *In situ* powder X-ray diffraction (PXRD) measurements were used in this work.

Experimental section

Synthesis of materials

The materials studied in this work were synthesized according to the procedure described in the literature and reported in section 2 of the ESI.†^{24,35} The matching of experimental PXRD with the simulated diffractograms of both materials are shown in Fig. S3 of section 3, ESI.†

In situ powder X-ray diffraction measurements and structural refinements

In situ powder X-ray diffraction (PXRD) was used to determine the structural changes in the architecture for both compounds during the water sorption processes. For this purpose, a Bruker D8 Advance diffractometer of Davinci design with a Bragg Brentano geometry equipped with a copper anticathode of $\text{K}\alpha$ line and a nickel filter and

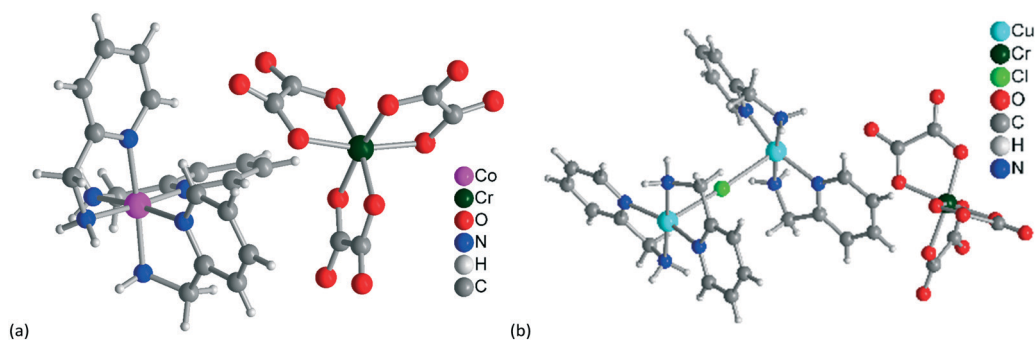


Fig. 1 Molecular metal complex building units of (a) $[\text{Co}(\text{amp})_3][\text{Cr}(\text{ox})_3]$ in **I'** and **I** and (b) $[\text{Cu}_2(\text{amp})_4\text{Cl}][\text{Cr}(\text{C}_2\text{O}_4)_3]$ in **II'** and **II**.

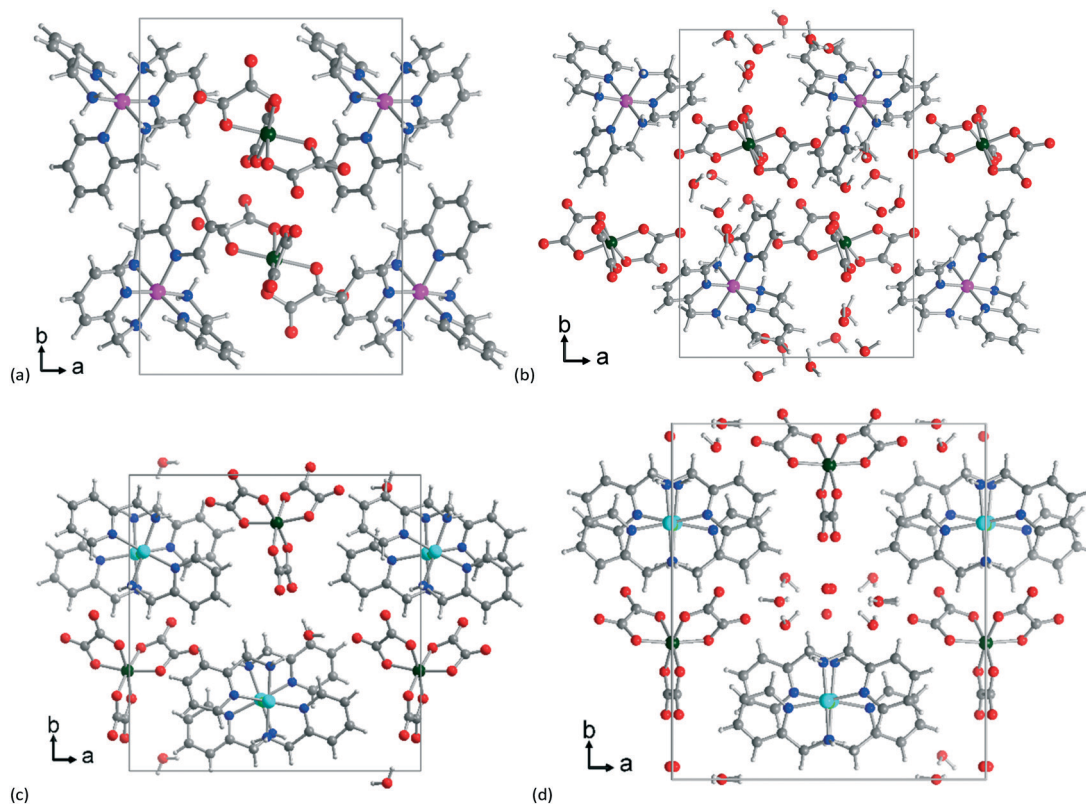


Fig. 2 Sections of the packing diagrams of (a) $[\text{Co}(\text{amp})_3][\text{Cr}(\text{ox})_3]$ (I'), (b) $[\text{Co}(\text{amp})_3][\text{Cr}(\text{ox})_3]\cdot 6\text{H}_2\text{O}$ (I), (c) $[\text{Cu}_2(\text{amp})_4\text{Cl}][\text{Cr}(\text{ox})_3]\cdot 1\text{H}_2\text{O}$ (II') and (d) $[\text{Cu}_2(\text{amp})_4\text{Cl}][\text{Cr}(\text{ox})_3]\cdot 6\text{H}_2\text{O}$ (II). I' and I differ mostly in the *a* and *b* axes, and II' and II mainly in the *b* axis, with the hydrated forms I and II having the longer axes (Fig. 2b and d and Table S3 of section 3, ESI†).

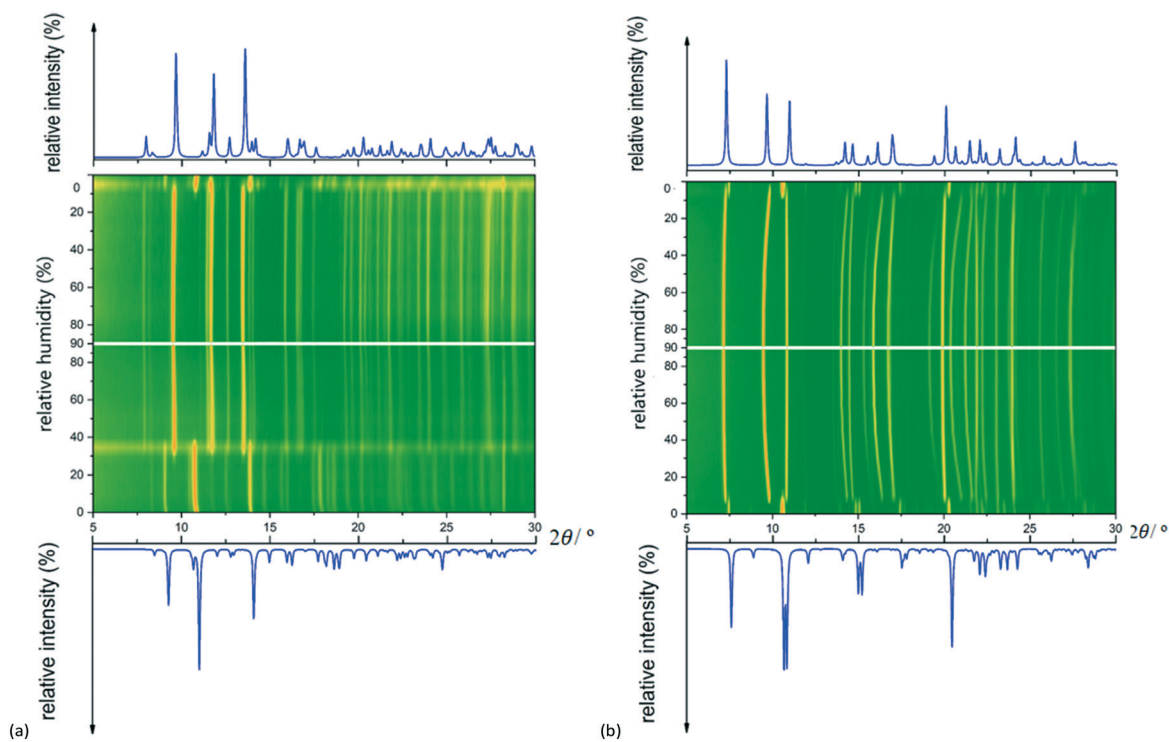


Fig. 3 PXRD carpet plots of I' (a) and II' (b) during the water adsorption and desorption processes in the humidity range from 0 to 88.1% r.H. and 88.1 to 0% r.H. at 40 °C, respectively. The starting and developing PXRD patterns correspond to (a) I' and I and (b) II' and II, respectively.

operating at a voltage of 40 kV and a current intensity of 40 mA was used. The samples were previously activated thermally at 100 °C for 3 h in agreement with the thermogravimetric analysis (TGA) results.²⁴ The activated materials (**I'** and **II'**) were then maintained at 40 °C in a nitrogen stream at different humidity levels between 0 and 88.1% r.H. during the water vapor adsorption and from 88.1 to 0% r.H. during desorption. These humidity levels were set and maintained at stable values using an Ansyco humidifier connected to an MRI temperature-controlled chamber in which the samples were measured. The measurements were done in the indicated humidity ranges with intervals of about 5% r.H. and 2θ steps of $0.02^\circ \text{ s}^{-1}$. The pattern matching refinements were carried out to determine the unit cell parameters of the material at all the humidity levels studied, as well as Rietveld refinements to quantify the phases present at the humidity levels for which mixtures were observed. The unit cell parameters obtained from the single crystal measurements were used as initial values, and all the refinements were carried out with the FullProf Suite program such that the structural models built showed PXRD patterns as close as possible to those obtained experimentally.^{24,35,36}

Results and discussions

Phase transitions occurring in **I'** and **II'** with humidity

Fig. 3(a) and (b) show the PXRD carpet plots of $[\text{Co}(\text{amp})_3][\text{Cr}(\text{ox})_3]$ (**I'**) and $[\text{Cu}_2(\text{amp})_4\text{Cl}][\text{Cr}(\text{C}_2\text{O}_4)_3]\cdot 1\text{H}_2\text{O}$ (**II'**), respectively, during adsorption (humidity range from 0 to 88.1% r.H.) and desorption (humidity range from 88.1 to 0% r.H.). The Bragg peaks indicate that the crystallinity of the materials was maintained after activation and preserved during the H_2O sorption process.

In compound **I'** the PXRD pattern does not change from 0% r.H. until 39% r.H. (Fig. 3a). At 30% r.H., additional new reflexes for compound **I** appear side by side to the previous reflexes of **I'**. The initial reflexes for **I'**, and the new reflexes for **I** match the simulated diffractograms. At 39% r.H. the reflexes of **I'** disappear, and only the reflexes of **I** remain. They are observed from this humidity level until 90% r.H. During the desorption process, the reflexes for **I** are observed from 90 to 5% r.H. but at 15% r.H. the reflexes observed for **I'** reappear. Such conversions were observed in the PXRD carpet plot diagram of $[\text{Cd}(\text{dbda})(\text{bipy})]\cdot 2\text{DMA}\cdot 2\text{H}_2\text{O}$ at temperatures varying from 25 to 300 °C.³⁷ This indicates that **I'** undergoes

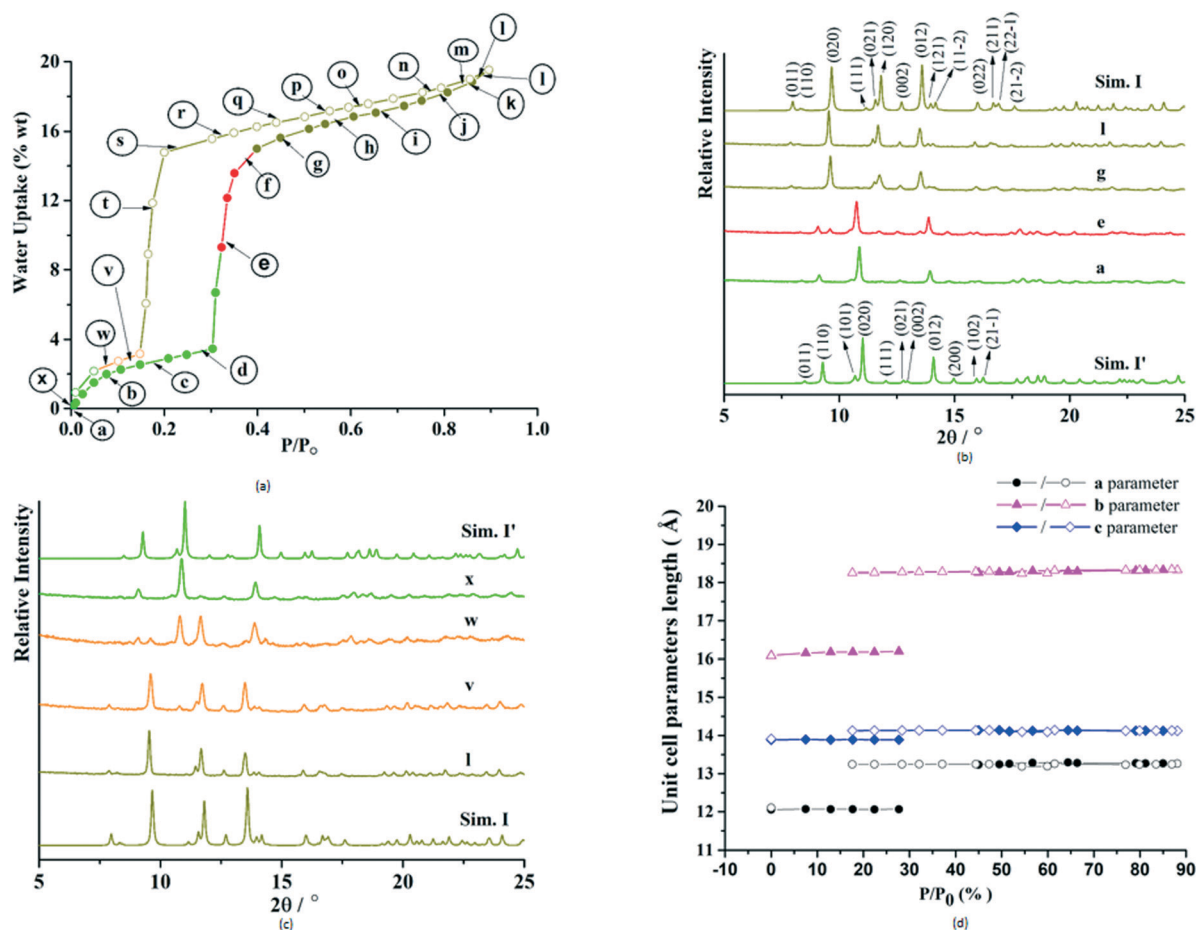


Fig. 4 (a) H_2O adsorption–desorption isotherms of **I'** at 40 °C, (b and c) its PXRD patterns in the range of $5 \leq 2\theta \leq 25^\circ$ at some selected relative humidity levels, respectively, during adsorption and desorption, and (d) variation of its unit cell parameters during both processes. For (a) and (d), the solid and open circles represent adsorption and desorption, respectively.

a discontinuous phase transition to **I** between 30 and 39% r.H. during the water adsorption process and between 15 and 5% r.H. during desorption. For both processes, the initial phase **I'** is converted into the second phase **I**, and at the end of the process only the phase **I** exists. The humidity values at which these structural transitions start during the adsorption-desorption processes are very close to the P/P_0 values at which the steep adsorption ($\sim 0.40 P/P_0$) and desorption ($\sim 0.15 P/P_0$) branches appear in the water sorption isotherm of the material (Fig. 4a).²⁴ The stepped isotherm for the water sorption of **I'** is thus related to these discontinuous phase transitions occurring during the water sorption process of this material as reported for ELM-11(Cu) and some compounds in the MIL-53 family.³⁸⁻⁴¹ This also explains why the carpet plot diagram of this material is not symmetrical and the large hysteresis loop found in its water sorption isotherm.

In compound **II'** the phase transition to **II** takes place between 7-10% r.H. upon adsorption and is also discontinuous like that in **I'**. Around 7% r.H., the reflexes for **II** appear and are observed up to 90% r.H. During the desorption process, the reflexes for **II** are observed from 90 to 3% r.H., and at 10% r.H., the reflexes for **II'** reappear. In **II'/II**

the phase transitions upon water adsorption and desorption start at a more similar humidity level than in **I'/I**, and this gives rise to a more symmetric carpet plot diagram in the former in agreement with the smaller hysteresis in its water vapor sorption isotherms (Fig. 5a).²⁴ The humidity levels at which both transitions start are also the same as the P/P_0 values (0.1) at which the steep adsorption branch starts and the desorption branch ends in the water sorption isotherm of the material (Fig. 5a). Remarkably both supramolecular structures, which are built from a metal complex cation and anion, exhibit a sudden reversible structural transformation, initiated by increasing/decreasing relative humidity, that is, discontinuous structural transitions of their architectures. However, in contrast to that of **I'**, the carpet plot diagram of **II'** shows lens-shaped diffraction lines (in the region 10 to 90% r.H.) in which some of them are more curved than others (see Fig. 3b). At 10% r.H. the prominent lens-shaped reflexes for **II** are observed at 2θ values equal to 9.87, 16.37 and 21.00°, but these values gradually change with humidity, and the reflexes appear at 9.50, 15.87, and 20.37° at 90% r.H. indicating the 2θ changes of -0.37, -0.50 and -0.63°, respectively. Le Bail and Rietveld refinements were used to obtain a deeper insight into the structural changes in the

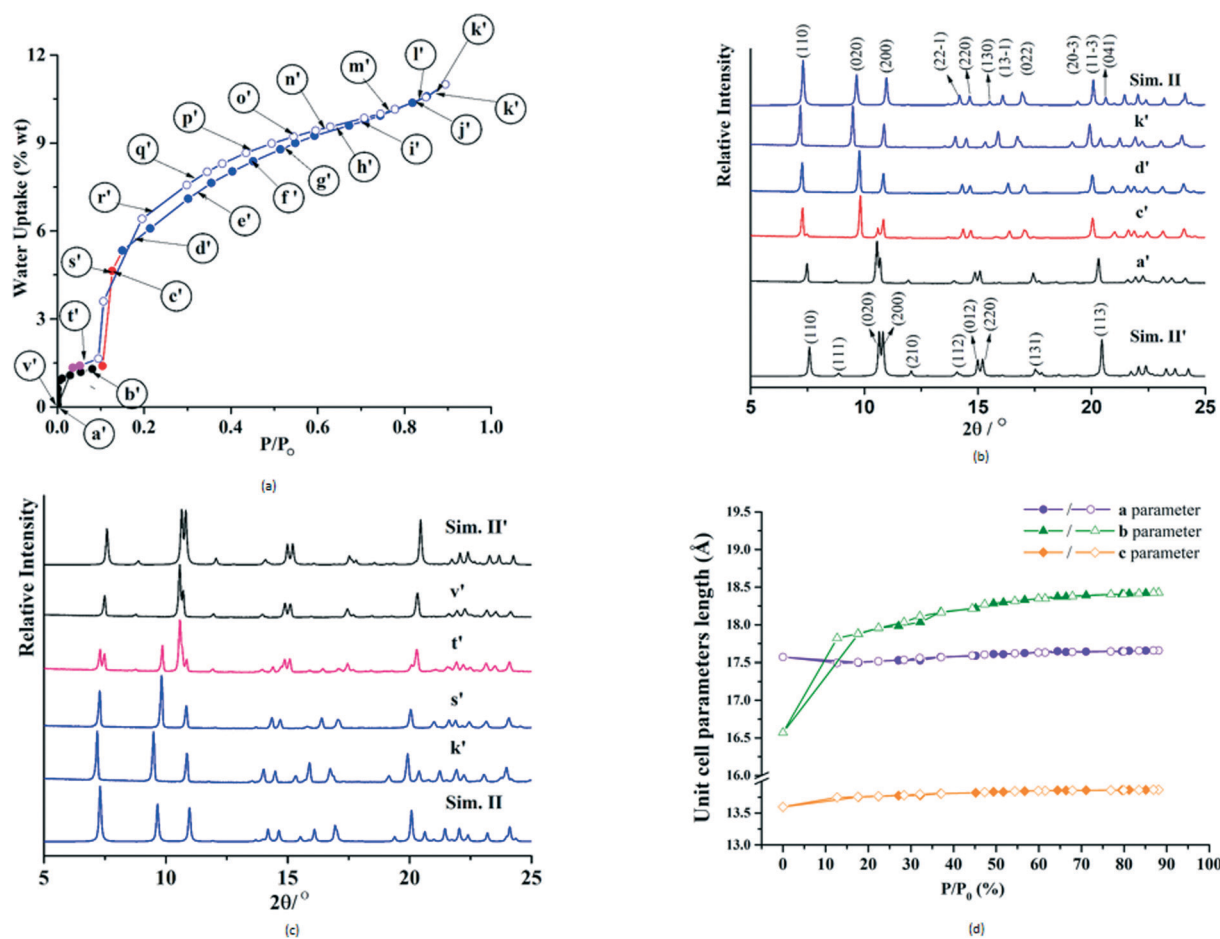


Fig. 5 (a) H_2O adsorption-desorption isotherms of **II'** at 40 °C, (b and c) its *in situ* PXRD patterns at some selected relative humidity levels, respectively, for adsorption and desorption added to those simulated from the structures of **II'** and **II**, and (d) variation of its unit cell parameters.

architectures of both materials **I'** and **II'** during these water adsorption–desorption processes.

Unit cell variation in **I'** and **II'** during the H₂O adsorption–desorption process

Fig. 4 shows the water adsorption–desorption isotherms of **I'** at 40 °C, its PXRD patterns measured at the same temperature respectively during the water adsorption and desorption processes together with those simulated from the structures of **I'** ([Co(amp)₃][Cr(ox)₃]) and **I** ([Co(amp)₃][Cr(ox)₃·6H₂O]), and the variation of its unit cell parameters during both processes (the values are given in Tables S5 and S6 of section 5, ESI†).

It is observed on Fig. 4(b) and (c) that at 0 and 88.1% r.H., the PXRD patterns of **I'** present the Bragg peaks similar to those simulated from the structures of **I'** ([Co(amp)₃][Cr(ox)₃]) and **I** ([Co(amp)₃][Cr(ox)₃·6H₂O]), respectively.³⁵ They both crystallized in the *P2₁/n* space group. The 2θ shift observed for all peaks arises from the zero offset of the detector. The unit cell parameters obtained with the Le Bail refinement of these patterns (see Tables S5 and S6, section 5 of ESI†) are very close to those obtained *via* single crystal measurements.³⁵ So, at 0% r.H., the material has the structure of [Co(amp)₃][Cr(ox)₃] (**I'**), and this structure is not changed up to 30% r.H. as it is confirmed with the value of the unit cell parameters in this range (see Fig. 4(d)). In this range, the material has adsorbed 1.3 mol of H₂O per mol of **I'** (steps **a** to **d** on Fig. 4(a)). This quantity is sufficient to provoke the discontinuous phase transition from the structure of **I'** to that of **I** which has bigger bilayer space (steps **d** to **f**). The rate of the conversion depends on the quantity of water vapor in the system. At 32.2% r.H. (step **e**), 14% of **I'** is transformed, while at 37.7% r.H. (step **f**) the rate is 60% (see parameters in section 6 of the ESI†). After this transition (steps **f** to **l**), **I'** does not exist anymore, and only **I** is present as observed in Fig. 4(b) and (d), even if the material adsorbs about 1.7 mol of H₂O per mol of **I'** in this range. During the desorption process (steps **l** to **t**), the structure of **I** is kept until the phase transition starts (15% r.H.). The quantity of water remaining in the material at this step is around 1.3 mol of H₂O per mol of **I'** similar to the quantity needed during the desorption process to stimulate the sudden adsorption of water. The conversion of the structure of **I** to that of **I'** is then taking place at the next humidity levels. Thus, the quantity of water molecules needed to initiate the phase transitions during both adsorption and desorption is around 1.3 mol of H₂O per mol of **I'**. Before this quantity, the material has the structure of **I'**, and after this quantity, it has that of **I**. During the discontinuous phase transition observed in this material, the space group is kept, and only the unit cell parameters are changed, particularly the *b* parameter, which changes from 16.08 to 18.34 Å (see Fig. 4(d)).

Similar observations were also made for **II'**. Its H₂O adsorption–desorption isotherms obtained at 40 °C is shown in Fig. 5, as well as its *in situ* PXRD patterns in the region of $5^\circ \leq 2\theta \leq 25^\circ$ together with those simulated from the structures of **II'** and **II** and the variation of its unit cell parameters during both processes (values are given in Tables S7 and S8 of ESI†).

As observed in this figure, the PXRD patterns of **II'** at 0% and 88.1% show peaks with 2θ values identical to those simulated from the structures of [Cu₂(amp)₄Cl][Cr(ox)₃]·1H₂O (**II'**) and [Cu₂(amp)₄Cl][Cr(ox)₃]·6H₂O (**II**), respectively. No supplementary peaks are observed in the measurement range, confirming that at 0% and 88.1% r.H. the material has the structure of **II'** and **II**, respectively. As **II'** crystallizes in the space group *P2₁/n*, while that of **II** is *C2/c*, this means that during the discontinuous phase transition occurring at 10% r.H. in the architecture of this material, its symmetry changes in contrast to that of **I'**. This explains the differences observed in the shifts of the diffraction lines in the PXRD carpet plot diagram of this material at the transition region. This kind of change is usually observed in flexible MOFs exhibiting a sudden increase in guest-accessible space.^{38–41} To the best of our knowledge, for the supramolecular porous networks exhibiting S-shaped isotherms reported in the literature, this property was not investigated. From 0 to 7.5% r.H. (steps **a'** to **b'**, Fig. 5(a)), the material has the structure of **II'** as shown in Fig. 5(b), and it adsorbs around 0.7 mol of H₂O per mol of **II'**. During the discontinuous phase transition, it adsorbs 2.1 mol of H₂O per mol of **II'** (step **b'** to **d'**), a quantity smaller than that of **I'** (4.5 mol of H₂O per mol of **I'**). In the range of 10 to 88.1% r.H., the material has the structure of **II** (step **d'** to **k'**), and the adsorption of water molecules in this range (2.9 mol of H₂O per mol of **II'**) is related to the continuous phase transition occurring with a gradual increase of the *b* parameter, while *a* and *c* remain almost stable (see Fig. 5(d)). During the desorption process the same phenomenon is observed from 88.1 to 10% r.H. (steps **k'** to **t'**), and this explains the lens-shape of the reflexes observed in the PXRD carpet plot of this material. The reflexes, with a gradual change in their 2θ positions with humidity from 10 to 90% r.H. by -0.37 , -0.50 and -0.63° indicated above, are indexed to (020), (13 $\bar{1}$) and (041), respectively. This change contrasts with the transformation observed in the architecture of **T12-apo**,⁴² a layered hydrogen-bonded organic framework during adsorption of CO₂ where a discontinuous phase transition occurred while a gradual gas uptake is observed. But, such a change is well known in the guest sorption process on the MIL-88 family of MOFs.¹⁷ The particularity in the case of **II'** is that this continuous transition occurred after the discontinuous one. This unusual mechanism was only reported for CO₂ sorption on **SHF-61-DMF** when one-third of the solvent content was removed.⁴³ This material comprises a doubly-interpenetrated anionic diamondoid framework with lozenge-shaped channels resembling those of MIL-53 and containing dimethylammonium cations. To the best of our knowledge, the combination of these flexibility modes was not yet reported with layered architectures.

Hydrogen bonds in the interlayer regions of **I'** and **II'**

The architectures of both materials have layers stacked along the *b* axis direction as shown in Fig. S1 and S2 of

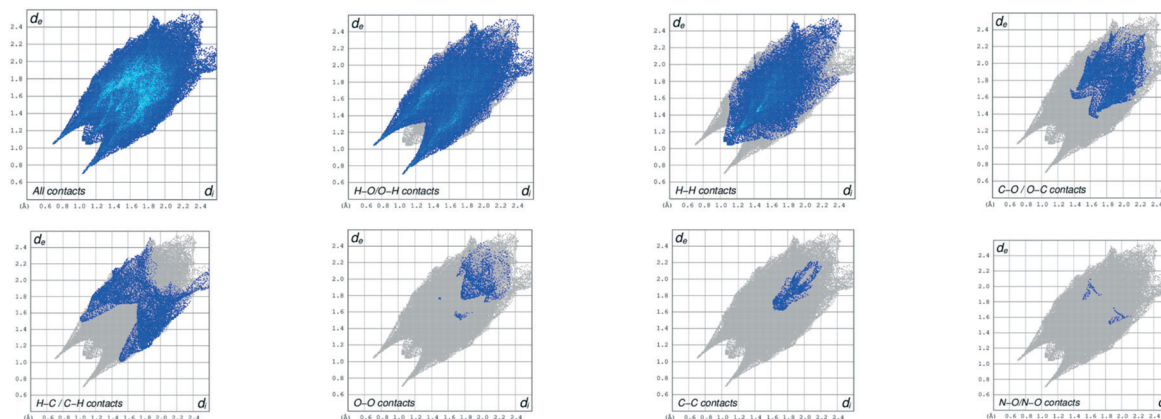


Fig. 6 2D fingerprint plots showing all contacts and O–H/H–O, H–H, O–C/C–O, H–C/C–H, O–O, C–C and N–O/O–N contacts, contributing to the Hirshfeld surface area of **I'**. These plots are made over d_{norm} ranging from 0.6697 to 1.5587 a.u. with the CrystalExplorer 17 program.⁴⁴

section 1 of the ESI.† Hydrogen bonds mainly contribute to this layered packing in both materials as shown in these figures, and this is confirmed by the 2D fingerprint plots of both materials (see Fig. 6 and 7). Indeed, the O–H/H–O contacts account for 50.5% of the total contribution to the Hirshfeld surface of **I'** and for 45.6% of that of **II'**. The other contacts in **I'** are H–H contacts (28.3%), C–O/O–C contacts (9.3%), H–C/C–H contacts (8.9%), O–O contacts (1.6%), C–C contacts (1.2%) and N–O/O–N contacts (0.1%). In **II'**, apart from the O–H/H–O contacts, other contributions to the Hirshfeld surface of this material come from the H–H contacts (27.6%), H–C/C–H contacts (15.1%), C–C contacts (4.8%), N–H/H–N contacts (2.1%), H–Cl/Cl–H contacts (1.8%), N–O/O–N contacts (1.2%), C–O/O–C contacts (1.8%), Cu–O/O–Cu (0.5%) and N–C/C–N contacts (0.2%). The 2D fingerprint plots showing these contributions to the Hirshfeld surface of both materials are given in Fig. 6 and 7. The list of hydrogen bonds which connect the layers in the architectures of both materials is given in Table 1, and they are drawn in Fig. S1 (for **I'**) and S2 (for **II'**) of section 1, ESI.†

In the architecture of **I'**, only two hydrogen bonds, namely, (N(3)–H(3B)···O(8) (2.777(8) Å, 141(8)°) and C(9)–H(9)···O(3) (3.150(7) Å, 128.5°), connect the layers, while six are involved in the architecture of **II'**. One of the six hydrogen bonds (C22–H22···O1 (3.033 (7) Å, 134°)) involve a carbon atom of the phenyl ring as a donor atom, while the five remaining ones connect the layers directly or indirectly (through the water molecule in the architecture of **II'**) with nitrogen or oxygen (in the case of the water molecule) as donor atoms (see Table 1). The mean value of the D···A lengths is 3.02 Å for these five hydrogen bonds. The comparison of the strength of these hydrogen bonds of the interlayer space of both materials shows that those involved in **I'** are stronger than those of **II'**. This can then explain why the gating effect is powerful in **I'** compared to **II'** and the gradual change which followed the gate effect in **II'**. Indeed, it is well known from the literature that the interactions between the layers decrease gradually as the interlayer space increases by gas adsorption.³¹ This interpretation is in agreement with the results obtained by Roztocki *et al.* in the study of the CO₂ sorption on 2D isophthalic- and 5-aminoisophthalic-MOFs.³⁴ Actually, sigmoidal isotherms

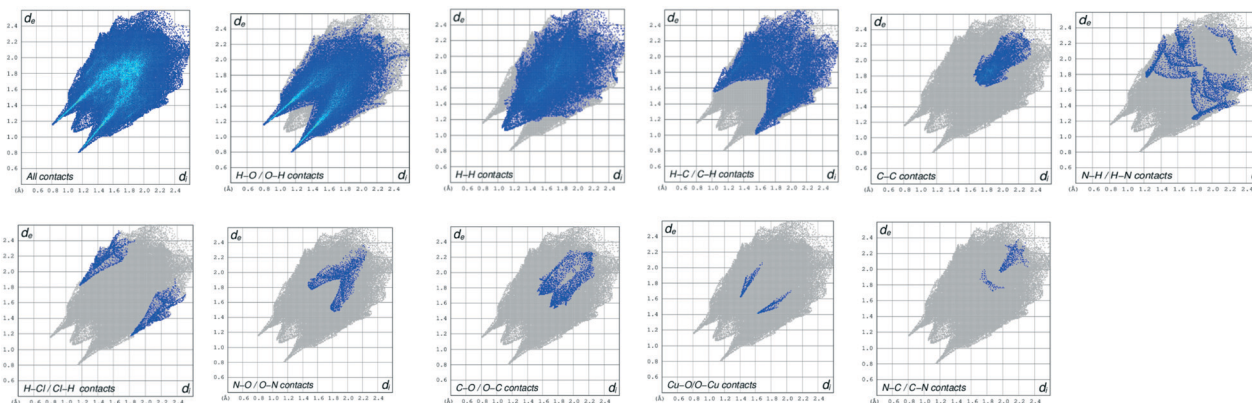


Fig. 7 2D fingerprint plots showing all contacts and O–H/H–O, H–H, H–C/C–H, C–C, N–H/H–N, H–Cl/Cl–H, N–O/O–N, C–O/O–C, Cu–O/O–Cu and N–C/C–N contacts, contributing to the Hirshfeld surface area of **II'**. The plots are made over d_{norm} ranging from 0.5087 to 1.6784 a.u., also with the CrystalExplorer 17 program.

Table 1 Hydrogen bond length (Å) and angles (°) in the interlayer region for **I'** and **II'**^{24,35}

D-H...A	D-H (Å)	H...A (Å)	D...A (Å)	D-H...A (°)
I'				
N(3)-H(3B)...O(8) ⁱ	0.86 (8)	2.05 (9)	2.777 (8)	141 (8)
C(9)-H(9)...O(3) ⁱⁱ	0.93	2.48	3.150 (7)	128.5°
II'				
O1W-H2W...O6 ^v	0.87	2.18	3.017 (6)	161.3
O1W-H1W...O2 ^{iv}	0.98	2.06	3.011 (7)	164.9
N1-H1B...O1W	1.02 (6)	2.04 (6)	3.038 (7)	165 (5)
N8-H8A...O1 ⁱ	0.82 (6)	2.25 (6)	3.012 (6)	157 (5)
N3-H3A...O10 ⁱ	0.88 (5)	2.19 (5)	2.973 (5)	147 (4)
C22-H22...O1 ⁱⁱⁱ	0.93	2.32	3.033 (7)	134

Symmetry codes for **I'**: i) $-x, -y, -z + 1$, ii) $-x + 1/2, y + 1/2, -z + 3/2$. Symmetry codes for **II'**: (i) $-x + 1, -y, -z + 1$; (iii) $-x + 1/2, y + 1/2, -z + 3/2$; (iv) $x + 1/2, -y + 1/2, z + 1/2$; (v) $-x + 1, -y + 1, -z + 1$.

were observed for MOFs having amino-substituted linkers, while no steps were observed for MOFs with unsubstituted linkers.

Conclusions

The structural changes occurring in the architecture of two 2D layered metal hydrogen-bonded organic frameworks, namely, [Co(amp)₃][Cr(ox)₃] (**I'**) and [Cu₂(amp)₄Cl][Cr(ox)₃]·1H₂O (**II'**), during their water sorption process were determined, and the strength of the interactions of the bilayer space of their architecture was analyzed. *In situ* powder X-ray diffraction (PXRD) was used for this purpose. The results show that the stepped water sorption isotherms on both materials are related to the discontinuous phase transitions, along which for **I'** the symmetry of the architecture is kept (space group $P2_1/n$) while for **II'** the symmetry is changed in the same crystallographic system ($P2_1/n$ to $C2/c$). In **II'**, this discontinuous phase transition is followed by a continuous change showing lens-shaped patterns in its PXRD carpet plot diagram. In both materials, all the changes mainly occur along the *b* axis direction of the stacking of layers. The gate effect occurs in **I'** at higher water pressure (30% r.H.) compared to that of **II'** (10% r.H.), and it contributes for water adsorption of 4.5 mol per mol of **I'** compared to 2.1 mol per mol of **II'**. All these differences can be ascribed to the strength of the H-bonds which connect the layers in both architectures. Those found in **I'** are stronger than those of **II'**. This suggest that stronger hydrogen bonds in the interlayer space in these layered materials are susceptible to drive a strong gate opening/closing effect and weaker interactions, a weaker effect or swelling effect.

Author contributions

PKT designed the study, synthesized the materials, checked their formulation and wrote the draft of the manuscript. YTSN performed the Le Bail and Rietveld refinements under the supervision of PKT and FP. FP also revised the first

manuscript draft. LR and DF carried out the *in situ* powder X-ray diffraction measurements. DF also contributed in the interpretation of the carpet plot diagrams. EH determined the water sorption properties of the two materials. CJ designed the work and edited the manuscript. All authors gave the final approval for publication and agreed to be held accountable for the work performed therein.

Conflicts of interest

The authors declare no competing interest.

Acknowledgements

The Third World Academy of Science (TWAS) and the German Science Foundation (DFG) are thanked for financial support of this work under the TWAS-DFG Visits Programme (Grant No. Ja-466/38-1). The authors gratefully acknowledge the financial support of the Federal German Ministry of Education and Research (BMBF) in the project Optimat under Grant No. 03SF0492C. We also thank the International Union Crystallography (IUCr) and the Cambridge Crystallographic Data Center (CCDC) for the promotion of crystallography and structural studies in Africa and particularly at the University of Dschang (Cameroon) through the IUCr Africa Initiative and FAIRE programmes, respectively.

References

- X. Jiang and H. Z. Kou, *Chem. Commun.*, 2016, **52**, 2952–2955.
- A. I. Cooper, *ACS Cent. Sci.*, 2017, **3**, 544–553.
- O. M. Yaghi, G. Li and H. Li, *Nature*, 1995, **378**, 703–706.
- T. J. M. Ma Ntep, H. Reinsch, J. Liang and C. Janiak, *Dalton Trans.*, 2019, **48**, 15849–15855.
- S. Dey, A. Bhunia, H. Breitzke, P. B. Groszewicz, G. Buntkowsky and C. Janiak, *J. Mater. Chem. A*, 2017, **5**, 3609–3620.
- A. Bhunia, S. Dey, M. Bous, C. Zhang, W. V. Rybinski and C. Janiak, *Chem. Commun.*, 2015, **51**, 484–486.
- M. Simard, D. Su and J. D. Wuest, *J. Am. Chem. Soc.*, 1991, **113**, 4696–4698.
- R.-B. Lin, Y. H. P. Li, H. Wang, W. Zhou and B. Chen, *Chem. Soc. Rev.*, 2019, **48**, 1362–1389.
- P. Brunet, M. Simard and J. D. Wuest, *J. Am. Chem. Soc.*, 1997, **119**, 2737–2738.
- H.-L. Wang, X.-F. Ma, Z.-H. Zhu, Y.-Q. Zhang, H. H. Zou and F.-P. Liang, *Inorg. Chem. Front.*, 2019, **6**, 2906–2913.
- Z. Bao, D. Xie, G. Chang, H. Wu, L. Li, W. Zhou, H. Wang, Z. Zhang, H. Xing, Q. Yang, M. J. Zaworotko, Q. Ren and B. Chen, *J. Am. Chem. Soc.*, 2018, **140**, 4596–4603.
- Z.-H. Zhu, H. L. Wang, H. H. Zou and F. P. Liang, *Dalton Trans.*, 2020, **49**, 10708–10723.
- J. M. Peng, H.-L. Wang, Z. H. Zhu, Z. Y. Liu, H. H. Zou and F.-P. Liang, *J. Mater. Chem. C*, 2021, **9**, 9319–9324.

- 14 J.-H. Deng, J. Luo, Y.-L. Mao, S. Lai, Y. N. Gong, D.-C. Zhong and T. - B. Lu, *Sci. Adv.*, 2020, **6**, 9976–9985.
- 15 R. Bruno, T. F. Mastropietro, G. D. Munno and D. Armentano, *Molecules*, 2021, **26**, 4594–4603.
- 16 S. Kitagawa and M. Kondo, *Bull. Chem. Soc. Jpn.*, 1998, **71**, 1739–1753.
- 17 C. Mellot-Draznieks, C. Serre, S. Surblé, N. Audebrand and G. Férey, *J. Am. Chem. Soc.*, 2005, 16273–16278.
- 18 R. Kitaura, K. Seki, G. Akiyama and K. Kitagawa, *Angew. Chem., Int. Ed.*, 2003, **42**, 428–431.
- 19 S. Biswas, S. Couck, D. Denysenko, A. Bhunia, M. Grzywa, J. F. M. Denayer, D. Volkmer, C. Janiak and P. Van Der Voort, *Microporous Mesoporous Mater.*, 2013, **181**, 175–181.
- 20 P. Abdolalian and A. Morsali, *Polyhedron*, 2019, **161**, 56–62.
- 21 D. Fairen-Jimenez, S. A. Moggach, M. T. Wharmby, P. A. Wright, S. Parsons and T. Duren, *J. Am. Chem. Soc.*, 2011, **133**, 8900–8906.
- 22 D. Fröhlich, S. K. Henninger and C. Janiak, *Dalton Trans.*, 2014, **43**, 15300–15304.
- 23 J. Ehrenmann, S. K. Henninger and C. Janiak, *Eur. J. Inorg. Chem.*, 2011, **2011**, 471–474.
- 24 P. K. Tsobnang, E. Hastürk, D. Fröhlich, E. Wenger, P. Durand, J. N. Lambi, C. Lecomte and C. Janiak, *Cryst. Growth Des.*, 2019, **19**, 2869–2880.
- 25 R. G. AbdulHalim, P. M. Bhatt, Y. Belmabkhout, A. Shkurenko, K. Adil, L. J. Barbour and M. Eddaoudi, *J. Am. Chem. Soc.*, 2017, **139**, 10715–10722.
- 26 J. Kim, W. Y. Kim and W. S. Ahn, *Fuel*, 2012, **102**, 574–579.
- 27 P. E. Quartapelle, T. Fukushima, E. Barea, J. A. R. Navarro, S. Horike and S. Kitagawa, *Chem. – Eur. J.*, 2012, **18**, 13117–13125.
- 28 A. Kondo, A. Chinen, H. Kajiro, T. Nakagawa, K. Kato, M. Takata, Y. Hattori, F. Okino, T. Ohba, K. Kaneko and H. Kanoh, *Chem. – Eur. J.*, 2009, **15**, 7549–7553.
- 29 J. Feng, H. Li, Q. Yang, S.-C. Wei, J. Zhang and C.-Y. Su, *Inorg. Chem. Front.*, 2015, **2**, 388–394.
- 30 T. Omiy, K. Sasaki, Y. Uchida and N. Nishiyama, *ACS Appl. Nano Mater.*, 2018, **1**, 3779–3784.
- 31 J. Yang, Q. Yu, Q. Zhao, J. Liang, J. Dong and J. Li, *Microporous Mesoporous Mater.*, 2012, **161**, 154–159.
- 32 L. Li, J. Yang, Q. Zhao and J. Li, *CrystEngComm*, 2013, **15**, 1689–1697.
- 33 R. Numaguchi, H. Tanaka, S. Watanabe and M. T. Miyahara, *J. Chem. Phys.*, 2014, **140**, 44707–44718.
- 34 K. Roztocki, M. Szufła, V. Bon, I. Senkowska, S. Kaskel and D. Matoga, *Inorg. Chem.*, 2020, **59**, 10717–10726.
- 35 P. K. Tsobnang, J. L. Ngolui, E. Wenger, P. Durand, S. Dahaoui and C. Lecomte, *Cryst. Growth Des.*, 2017, **17**, 4908–4917.
- 36 J. R. Carvajal, *Abstracts of the Satellite Meeting on Powder Diffraction of the XV Congress of the IUCr*, Toulouse, France, 1990, p. 127.
- 37 S. Lee, S. Jeong, J. Seong, J. Lim, A. Sharma, S. Won, D. Moon, S. B. Baek and M. S. Lah, *Mater. Chem. Front.*, 2021, **5**, 3621–3627.
- 38 A. Kondo, H. Noguchi, L. Carlucci, D. M. Proserpio, G. Ciani, H. Kajiro, T. Ohba, H. Kanoh and K. Kaneko, *J. Am. Chem. Soc.*, 2007, **129**, 12362–12363.
- 39 S. Bourrelly, P. L. Llewellyn, C. Serre, F. Millange, T. Loiseau and G. Férey, *J. Am. Chem. Soc.*, 2005, **127**, 13519–13521.
- 40 F. Millange, N. Guillou, R. I. Walton, J. M. Grenèche, I. Margiolaki and G. Férey, *Chem. Commun.*, 2008, 4732–4734.
- 41 V. Bon, I. Senkowska, D. Wallacher, A. Heerwig, N. Klein, I. Zizak, R. F. Dudzik and S. Kaskel, *Microporous Mesoporous Mater.*, 2014, **188**, 190–195.
- 42 I. Hisaki, S. Nakagawa, Y. Suzuki and N. Tohnai, *Chem. Lett.*, 2018, **47**, 1143–1146.
- 43 E. J. Carrington, C. A. McAnally, A. J. Fletcher, S. P. Thompson, M. Warren and L. Brammer, *Nat. Chem.*, 2017, **9**, 882–889.
- 44 M. J. Turner, J. J. McKinnon, S. K. Wolff, D. J. Grimwood, P. R. Spackman, D. Jayatilaka and M. A. Spackman, *CrystalExplorer17*, University of Western Australia, 2017.